https://doi.org/10.1016/j.isprsjprs.2017.04.012

Calibration of Boresight Offset of LROC NAC Imagery for Precision Lunar Topographic Mapping

Bo Wu*, Wai Chung Liu

Department of Land Surveying and Geo-Informatics, The Hong Kong Polytechnic University, Hung Hom, Kowloon, Hong Kong

* Corresponding author. Tel: +852 2766 4335; E-mail address: bo.wu@polyu.edu.hk.

Abstract **-** High-resolution and high-precision lunar topographic information is essential for lunar exploration and scientific research. The lunar surface imagery acquired by the Narrow Angle Cameras (NACs) of NASA's Lunar Reconnaissance Orbiter Camera (LROC) is a valuable dataset for lunar topographic mapping because of its very fine ground sampling distance (GSD) of 0.5-2 m. The NACs have a unique configuration consisting of two separate cameras closely mounted. This configuration enables the collection of lunar surface images with both large coverage and high resolution. However, the mapping results from the NAC images depend highly on the accuracy of the relative alignment (referred to as boresight offset) between the two NACs. This paper firstly presents the details of the NAC sensor configuration and orientations. Then, an approach to calibrate the boresight offsets of the two NACs is presented. By using triple-matching tie points between the NAC images, the boresight offsets are improved based on the geometric model through a least-squares adjustment. Experiments using typical NAC stereo images show that there are inconsistencies as great as 80 m in object space in the topographic models generated using the pre-flight determined SPICE kernels. The inconsistencies are well improved using the image orientation parameters derived from the temperature-dependent SPICE kernels recently released by the LROC team, however there are still small inconsistencies of about 5-10 m in object space, which can be further reduced to meter level by using the method proposed in this paper. This method is of significance for generating lunar topographic models with high precision and internal consistency from NAC imagery.

Keywords: Lunar Topography; LRO; LROC; NAC; Boresight Offset

1. Introduction

High-resolution and high-precision lunar topographic information is essential for lunar exploration missions and scientific research (Rosa et al., 2012; Di et al., 2014). Such information is commonly derived from lunar surface images using photogrammetric techniques. The Narrow Angle Cameras (NACs) of the NASA's Lunar Reconnaissance Orbiter Camera (LROC) provide images with a ground sampling distance (GSD) of 0.5-2 m (Robinson et al., 2010), far superior to other images. Moreover, LROC NAC imagery also offers very high geometric accuracy due to the precision orbit determination of the LRO spacecraft (Mazarico et al., 2013). Comparisons between the locations of surface hardware left from the Apollo and Soviet landers derived from stereo LROC NAC images and their true locations revealed a horizontal accuracy of better than 20 m (Speyerer et al., 2014).

The LROC NACs have a unique twin camera configuration comprising two separate cameras closely mounted on the optical bench, i.e., NAC Left (NACL) and NAC Right (NACR) (Figure 1), so that a single swath can provide lunar surface images with both large coverage and high resolution (e.g., ~5 km wide observation with a GSD of 0.5 m at an altitude of 50 km). This configuration depends greatly on the accuracy of the pointing alignments between the two cameras to reconstruct the actual scene being imaged. This relative alignment between NACL and NACR is referred to as the boresight offset. Although the boresight for each camera is measured in laboratory before the launch of the LRO, it is believed to be sensitive to extreme environmental changes while orbiting the Moon (Speyerer et al., 2014). It changes over time and must be modeled to remove inconsistencies in the derived topographic information or products.

Research to derive 3D topographic information, e.g., digital elevation models (DEMs) from LROC NAC imagery and the boresight problem, has attracted increasing attention. The

commercial software SOCET SET and the Integrated Software for Imagers and Spectrometers (ISIS) system developed by the United States Geological Survey (USGS) have been used to process the LROC NAC imagery for DEM generation (Robinson et al., 2012; Burns et al., 2012; Tran et al., 2010). Other in-house photogrammetric processing systems have also been used to derive DEMs from the LROC NAC imagery (Oberst et al., 2010; Li et al., 2011). Lin (2012) developed rigorous photogrammetric processing methods for LROC NAC imagery and separated the estimation of boresight parameters from the traditional bundle-adjustment process. Lin (2012) concluded that to avoid undesirable corrections, boresight estimation might not be included in the process of general bundle adjustment of image orientation parameters. Apart from highlighting the significance and potential of LROC NAC imagery for high-resolution lunar topographic modelling, one important message noted by researchers is that the continually varying boresight parameters are becoming one of the obstacles in high-precision lunar topographic mapping.

Speyerer et al. (2014) systematically investigated the pre-flight and on-orbit geometric calibration of the LROC NACs using thousands of NAC images. They found that the boresight offsets between the NACL and NACR are related to the sensor temperature when acquiring images. They developed a temperature-dependent model to provide improved image orientation parameters for NAC imagery.

Although the inaccurate boresight offsets could be improved in an integrated bundle adjustment process of the images, it is worthwhile to separately investigate the boresight offsets of the two NAC cameras and their influences on the mapping results. This paper presents a straightforward approach to calibrate the boresight offsets of the two NAC cameras to ensure correct relative orientation of them; so that to generate high-precision lunar topographic models.

2. Rigorous Modeling of LROC NAC Imagery

2.1 LROC NAC Sensor Configurations

The LROC NACs are designed to provide high-resolution monochrome imagery to locate safe landing sites for future robotic and human missions (Robinson et al., 2010, 2012). As illustrated in Figure 1 (a), the two NACs are separated and closely mounted on the optical bench. Each telescope has a diameter of 27 cm and the perspective centers of the two NACs are separated by about 33 cm. Each NAC uses a 5064-pixel charge-coupled device (CCD) line array providing a 2.85° field-of-view (FOV). The NACL is pointing 2.765° away (cross-track) from NACR so that the footprints of the two images overlap by about 135 pixels in the cross-track direction (Y-axis). This configuration allows the two NACs to provide a FOV of 5.7°, twice that of a single camera (Robinson et al., 2010; Bowman-Cisneros, 2010). The NACR is also mounted 0.106° forward of the NACL, with about 185 pixels separation in the along-track direction (X-axis) between the two images acquired by the NACs (Figure 1(b)). The NACL and NACR are mounted such that pixel 0 for the NACL is at the −Y end of its CCD and pixel 0 for the NACR is at the +Y end of its CCD (Figure 1(b)). This orientation requires that one of the NAC frames from a NACL and NACR paired observation must be transformed such that both images have the same ground orientation (Robinson et al., 2010).

Extraction of topographic information from the LROC NAC imagery requires stereo overlaps; stereo pairs are obtained by slewing the entire spacecraft to acquire off-nadir images from two adjacent orbits. Geometric stereo requires two images of the same terrain with a favorable convergence angle. The average NAC stereo pair has a convergence angle of 28.9° and an incidence angle change of 0.8° (Speyerer et al., 2014). The best temporal

resolution (time interval between two orbits) the LRO can achieve is about 2 hours (Robinson et al., 2010; Speyerer et al., 2014).

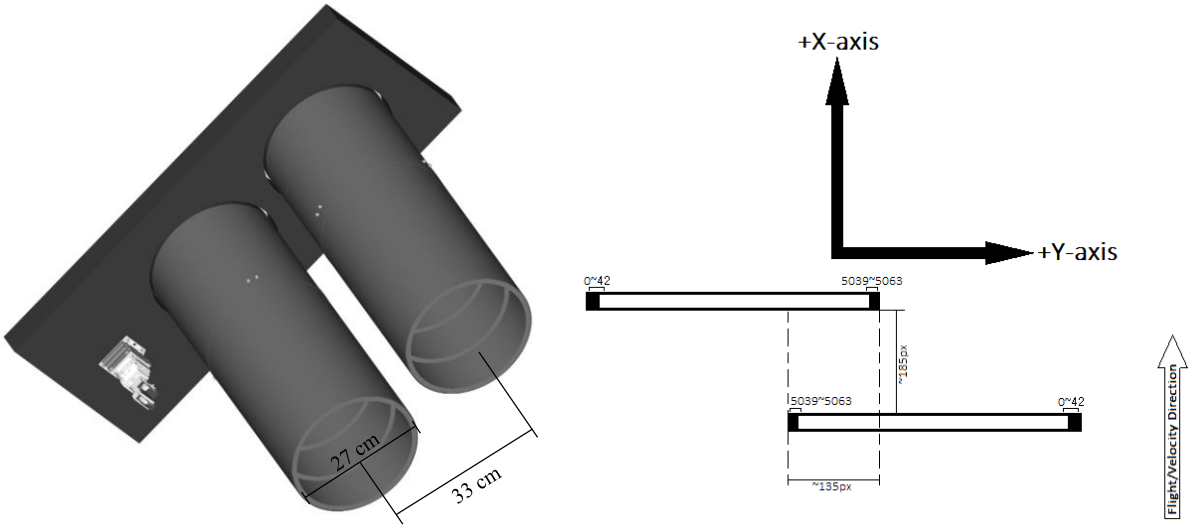

(a) (b)

Figure 1. Conceptual illustration of (a) the configuration of the LROC NACs and (b) the configurations of the NAC CCDs as mounted on the spacecraft (numbers show zero-based pixel addresses of the masked and non-imaging pixels) (Robinson et al., 2010).

2.2 Coordinate Frames

The coordinate frames in the LROC NAC sensor model include (1) the lunar body-fixed frame, (2) the LRO spacecraft frame, and (3) the NAC camera frame (Figure 2). The lunar body-fixed frame is defined by the Mean Earth/Polar Axis (ME) reference system with the origin located at the center of mass of the Moon, the Z-axis along the mean rotational pole, and the prime meridian in the mean Earth direction. Geographic locations of surface features can be expressed in planetocentric coordinates. In the present research, the exterior orientation parameters of NAC images are defined in the ME reference frame and the coordinates of lunar surface objects are expressed in planetocentric coordinates.

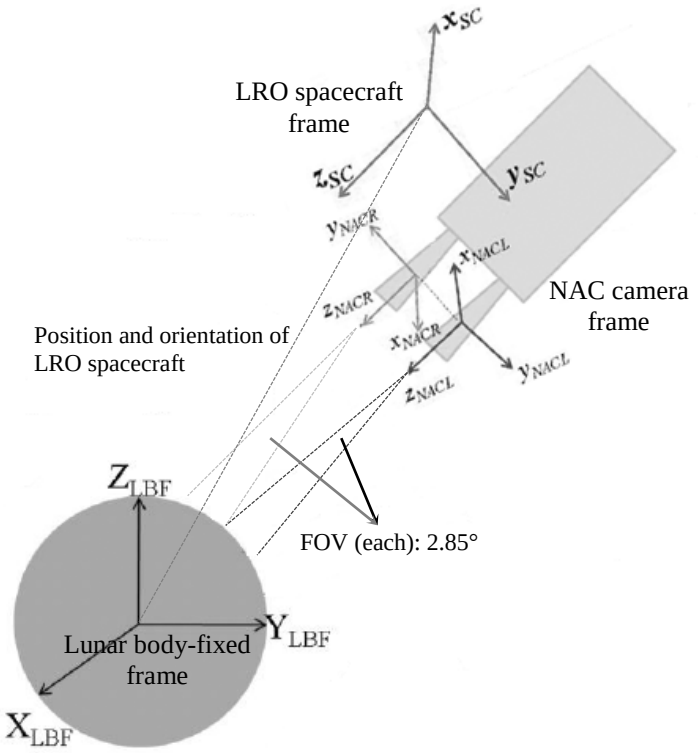

Figure 2. Coordinate frames including the Lunar body-fixed frame with subscript of "LBF", the LRO spacecraft frame with subscript of "SC", and the NAC camera frame with subscripts of "NACL" or "NACR".

The LRO spacecraft frame describes the position and orientation of the LRO spacecraft in the ME reference system. The origin of the LRO spacecraft frame is defined at the center of LRO interface with its X-axis parallel to the flight direction, the Y-axis in the cross track direction (right-hand rule), and the Z-axis pointing at the nadir. The NAC camera frame describes the image coordinates of the NAC images. The two NACs have nearly opposite viewing orientations and camera frames with respect to the LRO spacecraft frame.

The position and pointing information of LROC NAC are archived in a series of binary and text based Spacecraft, Planet, Instrument, C-Matrix and Events (SPICE) kernels. NASA's Navigational and Ancillary Information Facility (NAIF) maintains the SPICE ancillary information system (Acton, 1996). A series of spacecraft position kernels (SPKs),

C-matrix kernels (CKs), and a single frames kernel (FK) store the orientation parameters for the spacecraft and associated instruments (Speyerer et al., 2014).

2.3 Image Orientation

The image orientation includes interior orientation (IO), relative orientation between NACL and NACR, and exterior orientation (EO) of the images. IO parameters describe the intrinsic physical geometric properties of the sensor. They are provided in the SPICE instrument kernels as follows (Speyerer et al., 2014):

(1) Focal length: 699.62 mm for NACL and 701.57 mm for NACR.

(2) Pixel size (single CCD cell size) for both NACs: 7 μm.

(3) Boresight Sample (pixel): 2548 for NACL; 2496 for NACR.

The relative orientation between the NACL and NACR is denoted by boresight offsets including three translation offsets and three rotation angles. It should be noted that this research only focuses on the angular boresight offsets and the influences of the translational boresight offsets are ignored as they are negligible and unlikely to be variable on a detectable level.

Figure 3 illustrates the three angular boresight offsets. ω_b is the rotation angle of the boresight of NACL with respect to that of NACR around the X-axis (flight direction) in the NAC camera frame. φ_b is the rotation angle of the boresight of NACR with respect to that of NACL around the Y-axis. κ_b is the rotation angle of the boresight of NACL with respect to that of NACR around the Z-axis (nadir). This research examines two versions of the SPICE kernels of the LRO NAC imagery. One is the pre-flight standard version generated by the LRO Mission Operations Center (MOC) retrieved from NAIF website and the other is an improved version of temperature-dependent SPICE kernels as described in Speyerer et al.

(2014). The angular boresight offsets for the standard version of the SPICE kernels are fixed for all NAC images as follows: $\omega_b = -2.765°$, $\varphi_b = 0.106°$, and $\kappa_b = 180°$. The temperature-dependent SPICE kernels contain an updated frames kernel, an updated instrument kernel, and a series of new C-matrix kernels. They provide improved orientation parameters for NAC imagery, which are temperature dependent. The angular boresight offsets are therefore also temperature-dependent and varying for different NAC images. This research retrieves the improved orientation parameters for NAC imagery from ISIS 3.

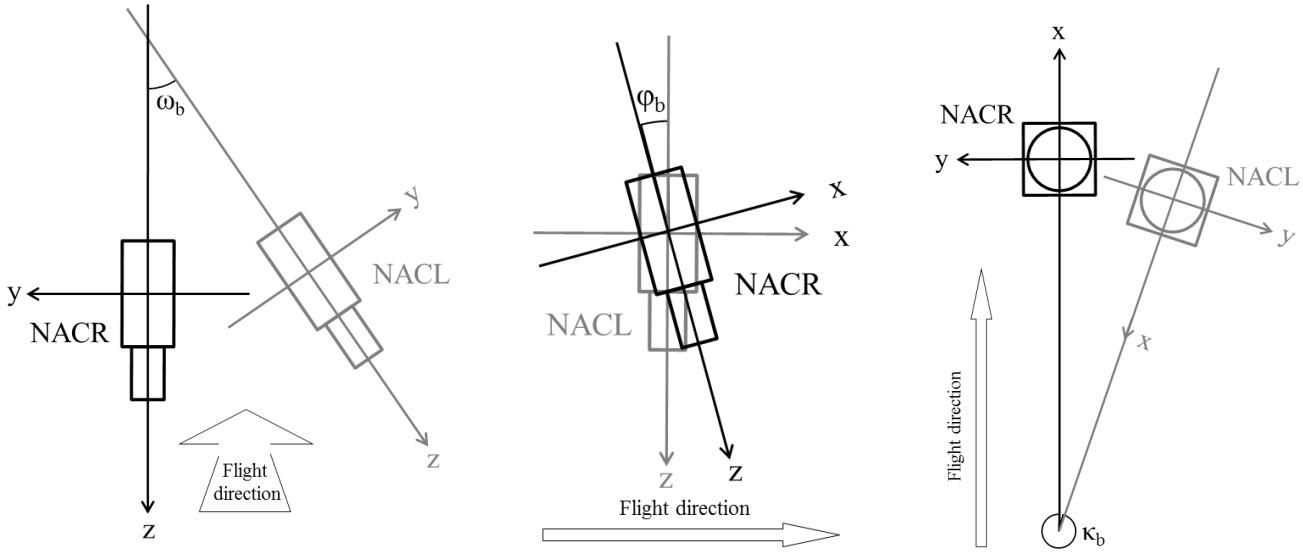

(a) (b) (c)

Figure 3. Conceptual illustration of the angular boresight offsets, (a) omega ω_b as viewing along the flight direction, (b) phi φ_b as viewing perpendicular to the flight direction, and (c) kappa κ_b as viewing pointing at the nadir.

EO parameters describe the position of the camera perspective center and the three pointing angles of the camera in the lunar body-fixed frame at the time of image acquisition. They can be retrieved from the SPICE kernels as mentioned previously. In this study, SPKs improved ("smithed" in ISIS terms) by the LOLA instrument team using crossover analyses are used to derive the positional information of the spacecraft (Mazarico et al., 2013).

Third-order polynomials are used to model the EO parameters of the NAC images as function of image rows (Li et al., 2011; Wu et al., 2011a, 2014a).

3. Calibration of Boresight Offsets of LROC NAC Imagery

3.1 Overview of the Approach

Usually a stereo pair of LROC NAC images consists of two orbits (i.e., O1 and O2) and two images (i.e., L and R) per orbit, resulting in a total of four images in the pair (O1L and O1R, O2L and O2R). There are six parameters of boresight offsets for each orbit of NACL and NACR images, of which three of them are translational offsets and the other three are angular offsets. Because the NACL and NACR are rigidly mounted on the optical bench with a distance of 33 cm (Figure 1), the possible variation of translational boresight offsets between them will be very small. The influences of translational boresight offsets on the mapping accuracy are unlikely to be variable on a detectable level. And according to Figure 4, the translational boresight offsets will have much less influences on the mapping accuracy compared with the angular ones, as the latter will be directly magnified by the orbit height. Therefore, this research only focused on the angular boresight offsets. Figure 4 illustrates the influence of an inaccurate boresight angle ω_b on the mapping accuracy, showing that an apparent elevation jump or dropping of ground points will appear in the overlapping area of O1R and O2L. The error is dependent on the orbit height. A 1-second error in ω_b results in a discrepancy in elevation of about 0.24 m in the elevation for an orbit height of 50 km. This, in return, has a serious effect on the accuracy of the object point coordinates.

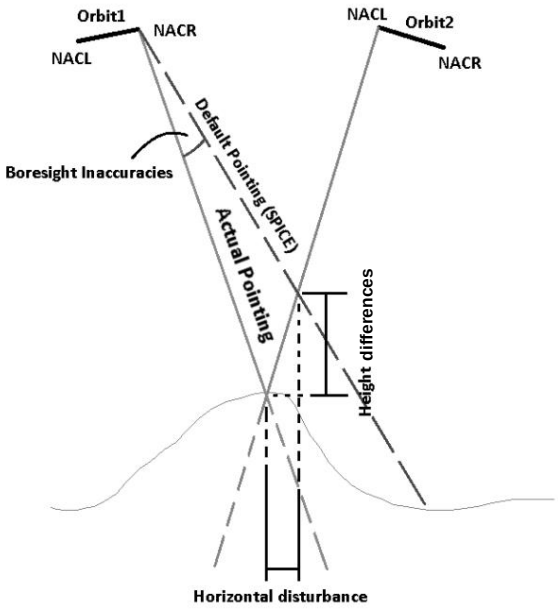

Figure 4. Illustration of the influences of inaccurate boresight angles on mapping accuracy.

The approach herein uses tie points obtained from the stereo images. Ideally, the 3D coordinates of the tie points calculated from different stereo combinations of the images should be consistent. However, this is not the case due to the errors in the boresight offsets. These errors or inconsistencies can be reduced or eliminated through a least-squares adjustment based on the geometric model of the NAC stereo images. The observations of the adjustment include the tie points, the 3D ground coordinates of the tie points, the boresight parameters, and the image EO parameters. Different weights are assigned to different observations. The outputs of the adjustment are the improved boresight offsets and improved image EO parameters, from which lunar topographic models with improved consistency and precision can be generated.

3.2 Determination of Tie Points

Because the overlapping region among the four images (2 NACL and 2 NACR) of the two stereo pairs is very narrow, it is rare to obtain quadruple-matching tie points from all the four

images. Instead, triple-matching tie points are more common to appear on the images. Therefore, triple-matching tie points are mainly used in the approach. Quadruple-matching tie points are also used if they are available and they are treated as two sets of triple-matching tie points in the process, but they are not necessary for the approach.

Figure 5 illustrates the triple-matching tie points used in the approach. They can be obtained from four types of image combinations, O1L-O1R-O2L, O1L-O1R-O2R, O2L-O2R-O1L, and O2L-O2R-O1R.

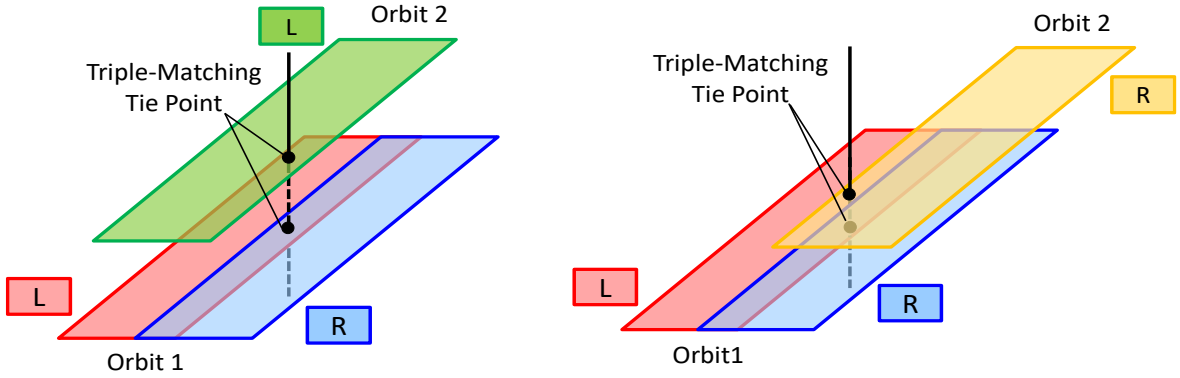

Figure 5. Illustration of triple-matching tie points, (a) triple-matching tie points between O1L, O1R, and O2L, and (b) triple-matching tie points between O1L, O1R, and O2R.

From Figure 5, it is apparent that the triple-matching tie points are always located along the overlapping region of the two NAC images (L and R) of the same orbit. We developed a self-adaptive triangle-constrained image matching (SATM) method for multiple images (Zhu et al., 2007, 2010; Wu et al., 2011b, 2012), which has been used to automatically obtain the triple-matching tie points in this research. To adapt for image matching in a relatively narrow overlapping area of the images, the matching area and search areas for matching are interactively determined during the image matching. Normally, dozens of triple-matching tie points can be matched for a stereo pair of NAC image sets through the SATM method.

3.3 Geometric Model and Process for Calibration of Boresight Offsets

For the LROC NAC stereo images, the relationship of a 3D ground point (X_p, Y_p, Z_p) and its corresponding pixel (x_p, y_p) can be represented by the following co-linearity equations:

$$\begin{aligned} x_p + \Delta x &= -f \frac{m_{11}(X_P - X_r) + m_{12}(Y_P - Y_r) + m_{13}(Z_P - Z_r)}{m_{31}(X_P - X_r) + m_{32}(Y_P - Y_r) + m_{33}(Z_P - Z_r)} \\ y_p + \Delta y &= -f \frac{m_{21}(X_P - X_r) + m_{22}(Y_P - Y_r) + m_{23}(Z_P - Z_r)}{m_{31}(X_P - X_r) + m_{32}(Y_P - Y_r) + m_{33}(Z_P - Z_r)} \end{aligned}, \quad (1)$$

where (X_r, Y_r, Z_r) are the coordinates of the camera perspective center in the lunar body-fixed frame dependent on the image row, f is the focal length of the camera, and m_{ij} are the elements of a rotation matrix that is determined entirely by the three rotation angles (ω, φ, and κ). The variables (X_r, Y_r, Z_r, ω, φ, and κ) are the EO parameters of the images. Δx and Δy are the polynomials with additional parameters to compensate for lens distortions. After linearization of Equations (2) and (1), the observation equation system can be represented in matrix form as follows:

$$\begin{aligned} V_1 &= AX_1 + BX_2 + CX_3 - L_1, \quad P_1 \\ V_2 &= \quad DX_2 \quad - L_2, \quad P_2 \\ V_3 &= EX_1 \quad - L_3, \quad P_3 \end{aligned}. \quad (2)$$

The observation equation system includes three types of observation equations. The first type is derived from the tie points in the images. They connect the 3D ground points and their image measurements by the EO parameters as indicated in Equations (1) and (2). X_1 is the vector of corrections to the EO parameters. Note that only the EO parameters for the NACR images are used here. The EO parameters for the NACL images are calculated from those of the NACR images based on the boresight offsets. X_2 represents the vector of corrections to the boresight offsets and X_3 denotes the vector of corrections to the unknown ground coordinates of the tie points. The coefficient matrices A, B, and C contain partial derivatives

with respect to the EO parameters, boresight offsets, and ground coordinates of the tie points. P_1 represents the weights for the tie points. As all the tie points are obtained through a reliable image matching method, their weights are assigned to be one-third of a NAC image pixel. L_1 is the observation vector of the tie points. V_1 is the vector of residual errors for this observation equation.

The second type is the pseudo-observation equation for the boresight offsets (three angular boresight offsets per orbit). The term "pseudo" indicates that the measurements are estimated and are not real measurements (such as the precisely matched tie points). They are used as initial values for the unknown angles. The coefficient matrix D contains partial derivatives with respect to the angular boresight offsets. P_2 represents their weights. The weights are estimated by analyzing the back-projection residuals of the inter-strip tie points of the two NACs in one orbit. As we do not expect dramatic changes to the angular boresight offsets, adjustments to them are allowed to change only by a small amount (e.g., in this study 0.1° for ω_b, φ_b, and κ_b, respectively). L_2 is the observation vector of the angular boresight offsets. V_2 is the vector of residual errors for this observation equation.

The third type is the pseudo-observation equation for the EO polynomial coefficients. The coefficient matrix E contains partial derivatives with respect to the EO polynomial coefficients, with P_3 representing their weights. L_3 is the corresponding observation vector and V_3 is the vector of residual errors for this observation equation. Including this observation equation allows for the refinement of the image EO parameters derived from the SPICE kernels. This is particularly useful for precision topographic modelling in bundle adjustment of image blocks involving multiple orbit images and non-standard stereo pairs (e.g., stereo images acquired with a time interval of several months rather than several hours) with more uncertainties in the image EO parameters. Note that the proportion of adjustment of each individual EO parameter can be controlled based on its corresponding weight. Normally,

relatively higher weights should be assigned to the position parameters compared to the angular parameters because of the latter's greater influence on the final mapping results. Applying infinitive weights to the position parameters, they will not change during the adjustment. It should be noted that from previous experiences in photogrammetry (Yoon and Shan, 2005; Wu et al., 2011a, 2014a), moderate changes in weight magnitude will yield the same results from the adjustment model.

Due to the nonlinearity of the collinearity equations in the model, linearization and initial values for all unknowns are prerequisites for performing the algorithm. The initial EO polynomial coefficients are computed through fitting with EO data derived from the standard SPICE kernels. The initial boresight offsets can be derived from the SPICE kernels. Subsequently, they are used to determine the initial ground coordinates for the tie points by photogrammetric space intersection. After the process, the refined EO parameters of the NACR images and the improved angular boresight offsets are obtained, from which the refined EO parameters of the NACL images can be derived. They will be used to generate lunar DEMs with improved consistency and precision through the photogrammetric process.

4 Experimental Analysis

4.1 Experimental Analysis using LROC NAC Image Set 1

The first experimental analysis uses a NAC stereo pair covering the Apollo 15 landing site with a range of 3.50º to 3.69º E and 25.59º to 26.53º N. Two orbits (1576 and 1577) of NAC images provide stereo coverage of the region. The north part of this region is relatively flat, but its south part belongs to the Mons Hadley Delta with a height increase of about 3 km. Part of the Hadley Rille passes the middle of the region. Figure 6 shows the stereo pair comprised of four images and the key image parameters.

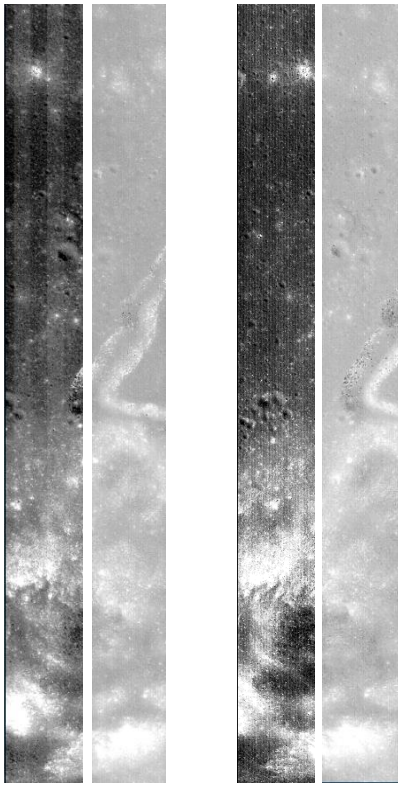

(a) (b)

Orbit number	1576	1577
Images	M111571816L/R	M111578606L/R
GSD	0.52 m	0.54 m
Slew angle	-13.506°	19.995°
Acquisition time	2009-10-30T19:55:49 to 2009-10-30T19:56:07	2009-10-30T21:48:58 to 2009-10-30T21:49:16

(c)

Figure 6. NAC image set 1, (a) orbit 1576, (b) orbit 1577, and (c) image specifications.

The NACL and NACR images for these two orbits have an obvious brightness difference as can be noticed in Figure 6 (a) and (b). The GSD for the images of the two orbits are slightly different, at 0.52 m and 0.54 m. The slew angle refers to the angle by which the camera pointing differs from the nadir in across-flight direction. The stereo configuration of the LROC NAC images is constructed from images on two orbits. The convergence angle of the stereo configuration determines the suitability of the image for inclusion in the photogrammetric process. Normally, a convergence angle exceeding 20° is optimal for precision topographic modelling, and that for this image set is 33.5°. Acquisition time refers to the time at which the image was captured. The images of these two orbits were taken with a time interval of about 2 hours.

The image orientation parameters derived from the standard version of SPICE kernels generated by the LRO MOC (here referred as standard SPICE kernels) are used to generate a DEM with a resolution of 1.5 m as shown in Figure 7 (a). It can be noticed from Figure 7 (a) that there are obvious differences in elevation along the midline in the region. This is mainly due to the inaccurate boresight parameters existing in the standard SPICE kernels.

The image orientation parameters derived from the temperature-dependent SPICE kernels released by the LROC team are also used to generate a DEM with the same resolution of 1.5 m as shown in Figure 7 (b). It can be seen that the differences in elevation have been relieved, which proves the improvement of the temperature-dependent SPICE kernels to the boresight parameters. However, there are still small discrepancies in the generated DEM.

The proposed method is used to improve the angular boresight offsets of the image set, and 65 triple-matching tie points are used. From the improved boresight offsets, improved image orientation parameters are obtained and they are used to generate a DEM with the same resolution of 1.5 m as shown in Figure 7 (c). It can be seen from Figure 7 (c) that the differences in elevation are gone and the terrain surface is smooth.

To quantitatively evaluate the performance of different approaches, discrepancies in object space and image space identified from the DEMs generated using the standard SPICE kernels, the temperature-dependent SPICE kernels, and after calibration of boresight offsets are calculated using all of the 65 tie points, as summarized in Table 1. The discrepancies in object space are denoted by the differences in ground coordinates of the same tie point obtained through photogrammetric intersection by using different image combination and their corresponding EO parameters. The discrepancies in image space are denoted by image residuals. The mean of the discrepancies is the mean of their absolute differences.

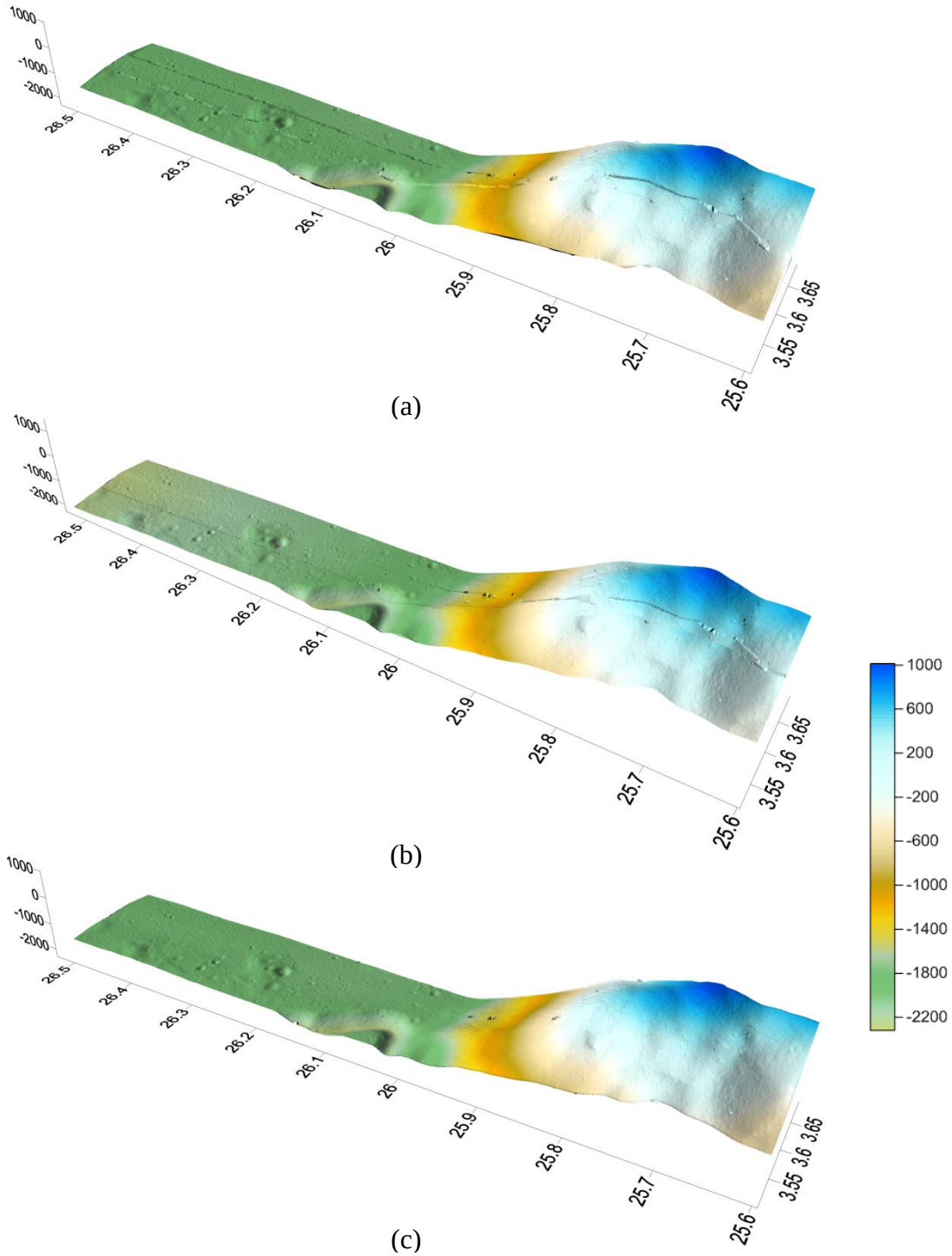

Figure 7. DEMs generated from NAC image set 1, (a) using the standard SPICE kernels, (b) using the temperature-dependent SPICE kernels, and (c) after improvement of boresight offsets.

Table 1. Discrepancies in the object and image spaces for NAC image set 1

		Discrepancies from the standard SPICE kernels			Discrepancies from the temperature-dependent SPICE kernels			Discrepancies after calibration of boresight offsets		
Object space		X (m)	Y (m)	Z (m)	X (m)	Y (m)	Z (m)	X (m)	Y (m)	Z (m)
	Mean	42.92	13.98	20.57	4.62	1.24	0.85	0.37	0.05	0.72
	Maximum	49.46	14.26	28.63	10.91	2.78	1.65	1.12	0.24	1.41
Image space		x (pixels)	y (pixels)		x (pixels)	y (pixels)		x (pixels)	y (pixels)	
	Mean	52.30	38.65		4.26	6.76		1.00	0.97	
	Maximum	52.94	45.21		9.41	12.87		1.87	3.88	

From Table 1, it can be noticed that the discrepancies in the DEM generated using the standard SPICE kernels are about 50 m in object space combining the three directions. The discrepancies have been reduced to about 5 m in the DEM generated using the temperature-dependent SPICE kernels. After calibration of boresight offsets, the discrepancies in the object space have been drastically reduced for all three directions (about 0.6 m combining the three directions). The discrepancies in image space also have the same trend, reduced from over 50 pixels when using the standard SPICE kernels to about 5 pixels using the temperature-dependent SPICE kernels. After calibration of boresight offsets, the image residuals have been drastically reduced to about one pixel for both the *x* and *y* directions.

Figure 8 provides a straightforward comparison of the orthorectified NACL and NACR image pairs generated using different ways. Figure 8 (a) is the orthorectified image pair for the entire image generated in ISIS 3 using the temperature-dependent SPICE kernels, which is used as reference for comparison. The Apollo 15 landing area is marked on the image using a rectangle. Figure 8 (b) is a close-up view of the Apollo 15 landing area in the

orthorectified image pair generated using the standard SPICE kernels. Obvious offsets between the orthorectified image pairs can be seen, as part of the right side of the NACR image is covered by the NACL image and the Apollo Lunar Surface Experiment Package (ALSEP) and the nearby tracks are almost missing in Figure 8 (b). This indicates the presence of errors in the boresight parameters between the two cameras. Figure 8 (c) is a close-up view of the Apollo 15 landing area in the orthorectified image pair generated in ISIS 3 using the temperature-dependent SPICE kernels. It can be seen that the offsets have been largely reduced. However, small offsets can still be noticed (the boundary of the crater below the ALSEP doesn't match in the NACL and NACR images). Figure 8 (d) is the close-up view of the Apollo 15 landing area in the orthorectified image pair generated after calibration of boresight offsets. It can be seen that the orthorectified NACL image is well aligned with the NACR image, which proves the effectiveness of the proposed approach.

To provide a check on the absolute accuracy of the mapping results from the NAC stereo imagery, the location of the Apollo 15 Laser Ranging Retroreflector (LRRR) visible in the NAC image (Figure 8 (d)) is obtained from the generated orthorectified image, which is 3.628532° E and 26.133293° N. Comparing with the ground truth data of 3.628507° and 26.133396° N (Williams et al., 2008) reveals an accuracy of better than 10 m, while the positional difference of LRRR between the two image pairs is 1.03 m (horizontal) and 0.62 m (vertical).

Figure 9 gives a detailed overview of the performance of proposed appraoch through profile comparison. Three profiles are selected for comparison (Figure 9 (a)). Their profiles on the DEMs generated using the standard SPICE kernels, the temperature-dependent SPICE kernels, and after calibration of boresight offsets are shown in Figure 9 (b), (c), and (d). The profiles on the DEM generated using the standard SPICE kernels show obvious elevation jumps or drops along the middle part of the profiles. The problem has been improved for the

profiles on the DEM generated using the temperature-dependent SPICE kernels. After calibration of boresight offsets, the problem has been well solved with no noticeable elevation jumps or drops existing on the profiles.

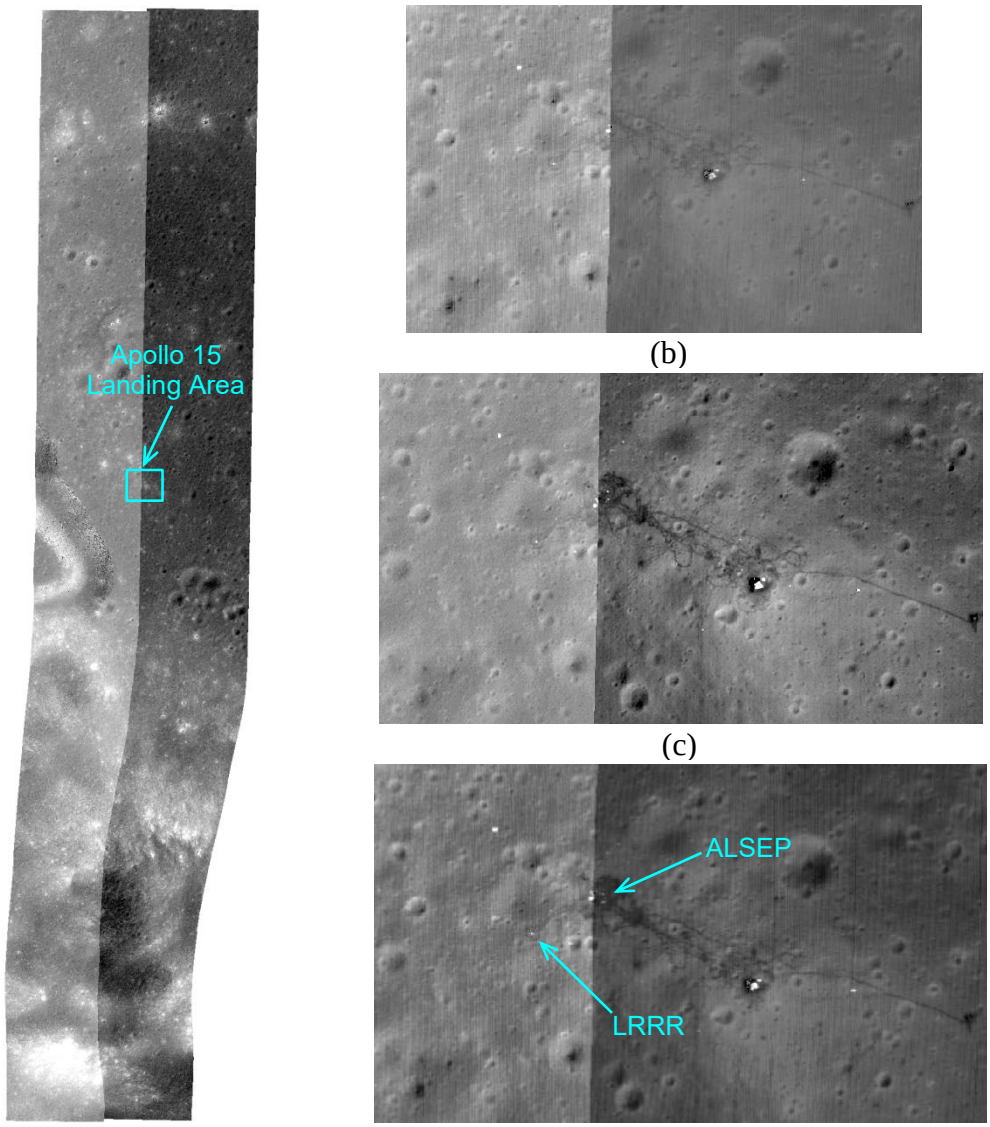

Figure 8. Comparison of orthorectified NACL and NACR image pair for image set 1. (a) Orthorectified image pair for the entire image (M111578606L/R) showing the Apollo 15 landing area, (b) a close-up view of the Apollo 15 landing area in the orthorectified image pair generated using the standard SPICE kernels, (c) using the temperature-dependent SPICE kernels, and (d) after calibration of boresight offsets.

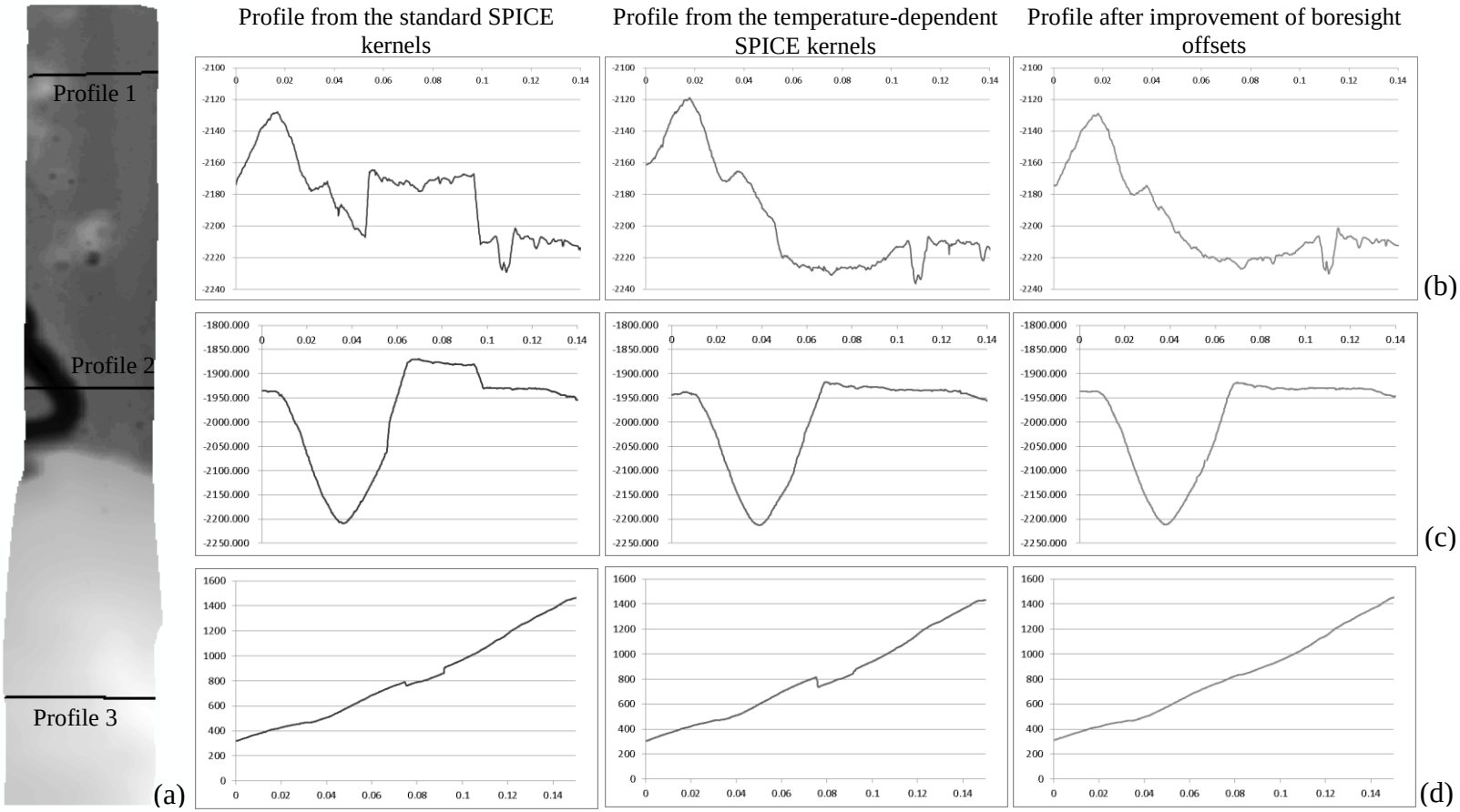

Figure 9. Profile comparison of the DEMs generated using different SPICE kernels for image set 1. (a) Three selected profiles marked on the planar view of the DEM, and comparisons for (b) profile 1, (c) profile 2, and (d) profile 3. (The units in the profile plots are meters of elevation for the vertical axis and degrees of longitude (with start point as 0°) for the horizontal axis)

4.2 Experimental Analysis using LROC NAC Image Set 2

The second experimental analysis uses a NAC stereo pair showing the lunar maria on the near side covering a region from 51.26º to 51.5º W and 43.6º to 44.56º N. Two orbits (10665 and 10666) of NAC images provide stereo coverage of the region. This region is relatively flat, with a valley about 1 km wide traversing the region. Figure 10 shows the stereo pair comprised of four images and the key image parameters.

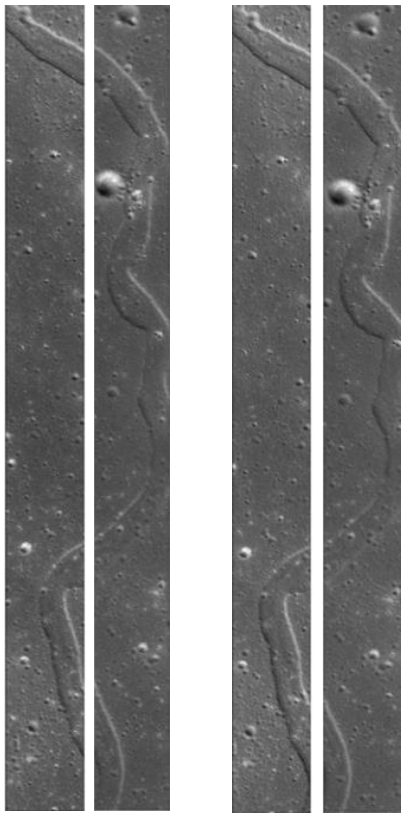

(a) (b)

Orbit number	10665	10666
Images	M173246166L/R	M173252954L/R
GSD	0.5 m	0.52 m
Slew angle	-17.539°	9.681°
Acquisition time	2011-10-14T15:41:38 to 2011-10-14T15:41:56	2011-10-14T17:34:46 to 2011-10-14T17:35:04

(c)

Figure 10. NAC image set 2, (a) orbit 10665, (b) orbit 10666, and (c) image specifications.

The GSD for the images are 0.5 m for orbit 10665 and 0.52 m for orbit 10666. The convergence angle for this image set is 27.22°. The images of these two orbits were taken with a time interval of about 2 hours. For this image set, both the spatial resolution and acquisition time interval are best-case values from the NAC image data sets.

Same with the previous experiment, DEMs are generated using the standard SPICE kernels, the temperature-dependent SPICE kernels, and after calibration of boresight offsets (32 triple-matching tie points are used) as shown in Figure 11.

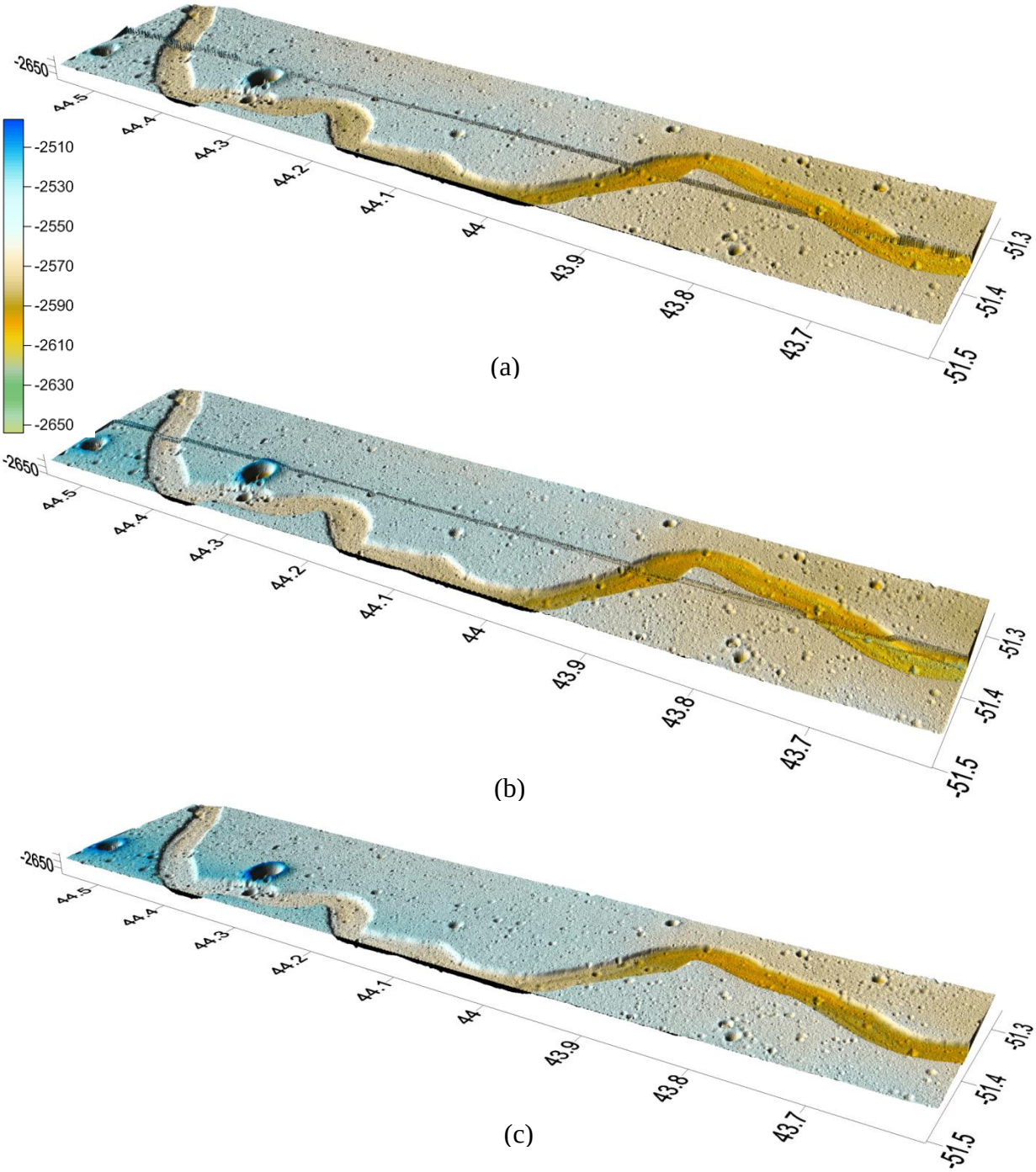

Figure 11. DEMs generated from NAC image set 2, (a) using the standard SPICE kernels, (b) using the temperature-dependent SPICE kernels, and (c) after improvement of boresight offsets.

As can be seen in Figure 11 (a), there are obvious differences in elevation along the midline in the region due to the inaccurate boresight angles. The situation has been improved in the DEM generated using the temperature-dependent SPICE kernels, as the disturbances are less obvious as shown in Figure 11 (b). After calibration of boresight offsets, the differences in elevation are gone and the terrain surface is smooth as shown in Figure 11 (c).

The discrepancies in object space and image space identified from the DEMs generated using different SPICE kernels are calculated and summarized in Table 2. Table 2 shows that the discrepancies in object space are about 80 m combining the *X*, *Y*, and *Z* in the DEM generated using the standard SPICE kernels. Using the temperature-dependent SPICE kernels, the discrepancies reduced to about 10 m in the DEM. The performance of the temperature-dependent SPICE kernels is less effective than the case in the previous experiment using the NAC images in the Apollo 15 landing area. After calibration of boresight offsets, the discrepancies in the object space have been drastically reduced to about 2 m combining the three directions. For discrepancies in image space, similar trends with those in the previous experiment can be found.

Table 2. Discrepancies in the object and image spaces for NAC image set 2

		Discrepancies from the standard SPICE kernels			Discrepancies from the temperature-dependent SPICE kernels			Discrepancies after calibration of boresight offsets		
Object space		X (m)	Y (m)	Z (m)	X (m)	Y (m)	Z (m)	X (m)	Y (m)	Z (m)
	Mean	36.10	45.93	54.53	5.21	6.73	6.48	1.00	1.12	1.61
	Maximum	53.85	57.36	56.52	7.07	12.23	10.92	2.37	2.00	2.39
Image space		x (pixels)	y (pixels)		x (pixels)	y (pixels)		x (pixels)	y (pixels)	
	Mean	77.65	4.94		9.71	4.92		1.00	0.52	
	Maximum	79.08	8.73		15.07	8.96		2.21	1.22	

Figure 12 provides a straightforward comparison of the orthorectified NACL and NACR image pairs generated using different ways. Figure 12 (a) is the orthorectified image pair for the entire image generated in ISIS 3 using the temperature-dependent SPICE kernels used as a reference. Figure 12 (b) is a close-up view of the region marked with the rectangle in Figure 12 (a), which is a subset of the orthorectified image pair generated using the standard SPICE kernels. Obvious offsets can be noticed as part of the right side of the NACR image is covered by the NACL image and the right part of the crater located around the center is missing. Figure 12 (c) is a close-up view of the same region in the orthorectified image pair generated in ISIS 3 using the temperature-dependent SPICE kernels. Obvious offsets can still be noticed referring to the shift of the crater boundaries on the NACL and NACR images. The offsets are gone in the orthorectified image pair generated after calibration of boresight offsets as shown in Figure 12 (d). The boundaries of the crater are well aligned on the NACL and NACR images.

Similarly, detailed profile comparison is carried out for this NAC image set and the results are shown in Figure 13. It clearly illustrates that the obvious elevation jumps or drops on the profiles from the DEMs generated using the standard SPICE kernels or using the temperature-dependent SPICE kernels are effectively eliminated after calibration of boresight offsets.

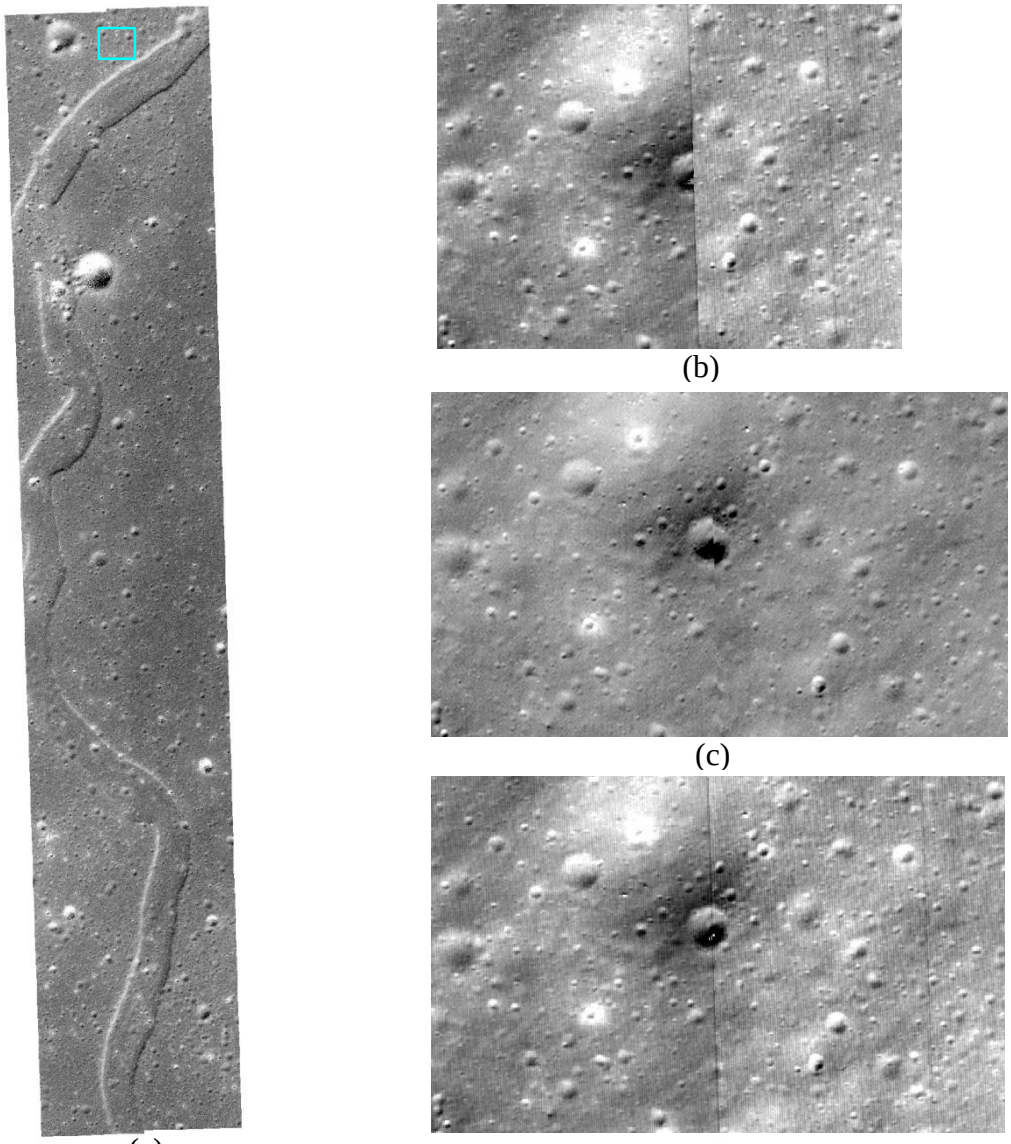

(a) (b) (c) (d)

Figure 12. Comparison of orthorectified NACL and NACR image pair for image set 2. (a) Orthorectified image pair for the entire image (M173246166L/R), (b) a close-up view of the region marked with a cyan rectangle in (a) in the orthorectified image pair generated using the standard SPICE kernels, (c) using the temperature-dependent SPICE kernels, and (d) after calibration of boresight offsets.

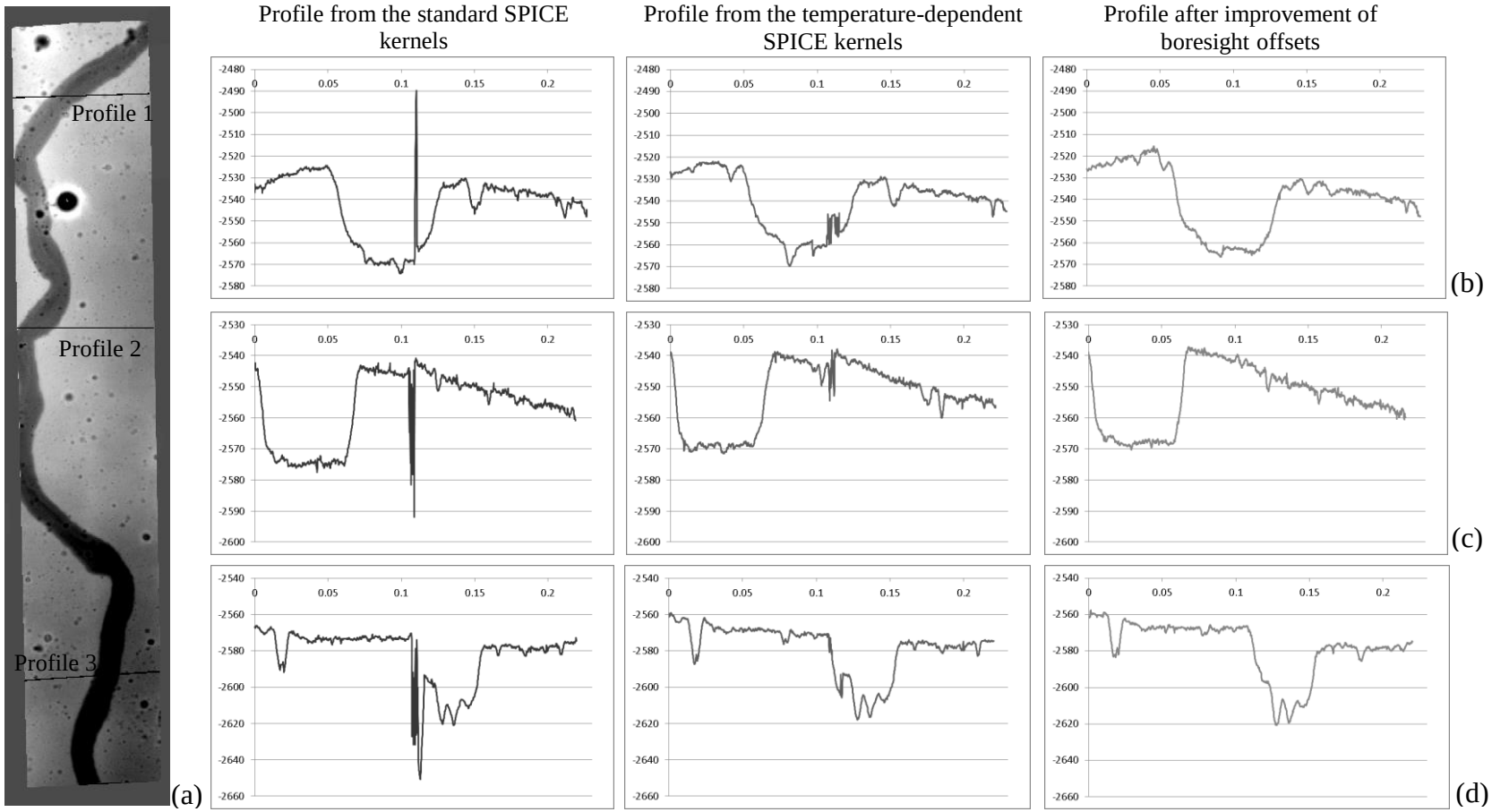

Figure 13. Profile comparison of the DEMs generated using different SPICE kernels for image set 2. (a) Three selected profiles marked on the planar view of the DEM, and comparisons for (b) profile 1, (c) profile 2, and (d) profile 3. (The units in the profile plots are meters of elevation for the vertical axis and degrees of longitude (with start point as 0°) for the horizontal axis)

4.3 Experimental Analysis using LROC NAC Image Set 3

The third experimental analysis uses a NAC stereo pair taken in the highland area close to the Sinus Iridum where the Chinese Chang'E-3 landed (Wu et al., 2013, 2014b). LROC NAC images from two orbits (10298 and 10299) provide stereo coverage of the region, ranging from 30.93° to 31.2° W and 48.1° to 48.99° N. This region has fluctuating terrain with an elevation range of 2.4 km. Figure 14 shows the stereo pairs comprised of four images and the key image parameters. The GSD for the images are 0.55 m for orbit 10298 and 0.52 m for orbit 10299. The slew angles for the two orbits are -18.889° and 3.581°, offering a convergence angle of 22.47°. The images were taken with a time interval of about 2 hours.

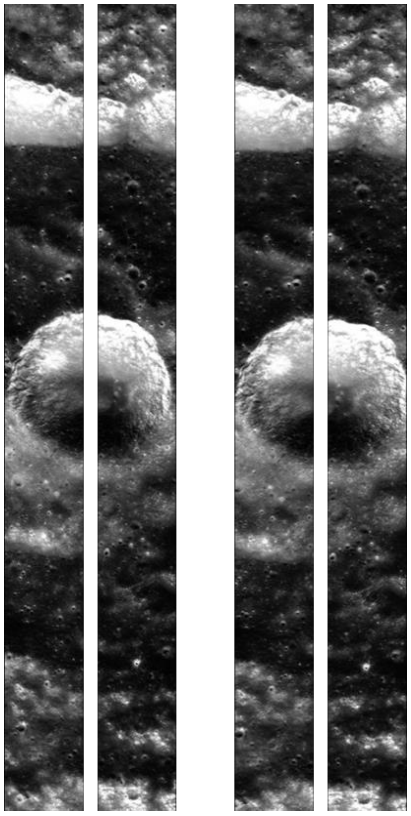

(a) (b)

Orbit number	10298	10299
Images	M170755060L/R	M170761847L/R
GSD	0.55 m	0.52 m
Slew angle	-18.889°	3.581°
Acquisition time	2011-09-15T19:43:12 to 2011-09-15T19:43:30	2011-09-15T21:36:19 to 2011-09-15T21:36:37

(c)

Figure 14. NAC image set 3, (a) orbit 10298, (b) orbit 10299, and (c) image specifications.

DEMs are generated using the standard SPICE kernels, the temperature-dependent SPICE kernels, and after calibration of boresight offsets (42 triple-matching tie points are used). Figure 15 shows the DEMs.

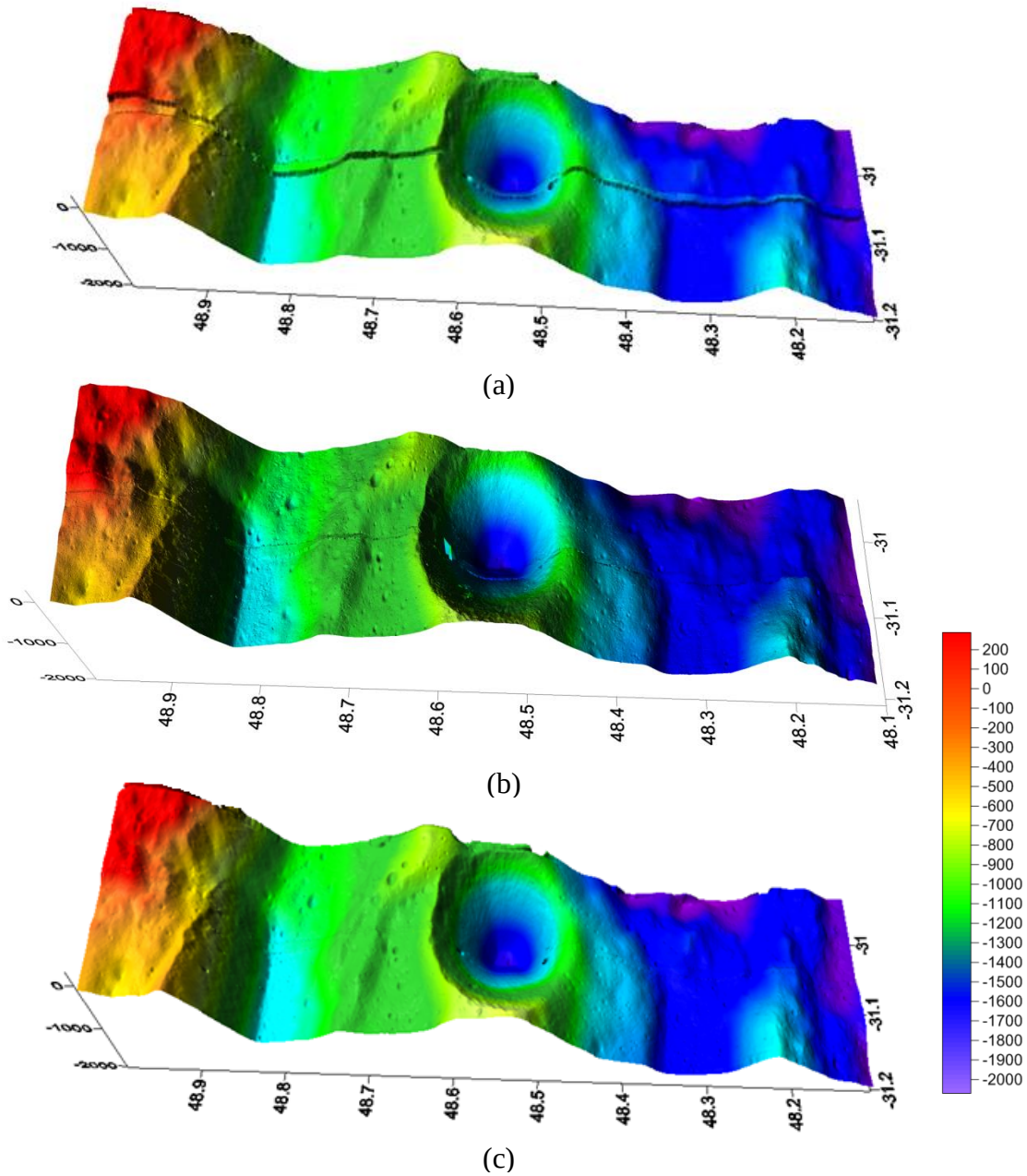

Figure 15. DEMs generated from NAC image set 3, (a) using the standard SPICE kernels, (b) using the temperature-dependent SPICE kernels, and (c) after calibration of boresight offsets.

As can be seen in Figure 15 (a), there are obvious differences in elevation along the midline in the region due to the inaccurate boresight angles. The situation has been well improved in the DEM generated using the temperature-dependent SPICE kernels, however there are still light scars visible in Figure 15 (b) indicating small differences in elevation. After calibration of boresight offsets, the differences in elevation are gone and the terrain surface is smooth as shown in Figure 15 (c).

The discrepancies in object space and image space identified from the DEMs generated from different ways are calculated and summarized in Table 3. Table 3 shows that the discrepancies in object space are about 70 m combining the *X*, *Y*, and *Z* directions in the DEM generated using the standard SPICE kernels. Using the temperature-dependent SPICE kernels, the discrepancies reduced to about 10 m combining the three directions in the DEM. After calibration of boresight offsets, the discrepancies in the object space have been drastically reduced to about 1 m combining the three directions. For discrepancies in image space, the image residuals have been drastically reduced from dozens of pixels to about one pixel after calibration of boresight offsets.

Table 3. Discrepancies in the object and image spaces for NAC image set 3

		Discrepancies from the standard SPICE kernels			Discrepancies from the temperature-dependent SPICE kernels			Discrepancies after calibration of boresight offsets		
Object space		X (m)	Y (m)	Z (m)	X (m)	Y (m)	Z (m)	X (m)	Y (m)	Z (m)
	Mean	42.57	17.06	53.89	7.32	2.39	8.48	0.37	0.20	0.56
	Maximum	56.04	26.35	62.65	10.81	7.91	16.28	0.85	0.59	1.47
Image space		x (pixels)	y (pixels)		x (pixels)	y (pixels)		x (pixels)	y (pixels)	
	Mean	52.66	34.54		9.01	4.03		1.08	0.58	
	Maximum	53.91	37.52		15.78	7.42		2.22	1.54	

Figure 16 provides a similar comparison of the orthorectified NACL and NACR image pairs with previous experiments. Again, obvious offsets can be noticed in the orthorectified image pair generated using standard SPICE kernels. The offsets are reduced in the orthorectified image pair generated using the temperature-dependent SPICE kernels and are finally eliminated in the orthorectified image pair after calibration of boresight offsets.

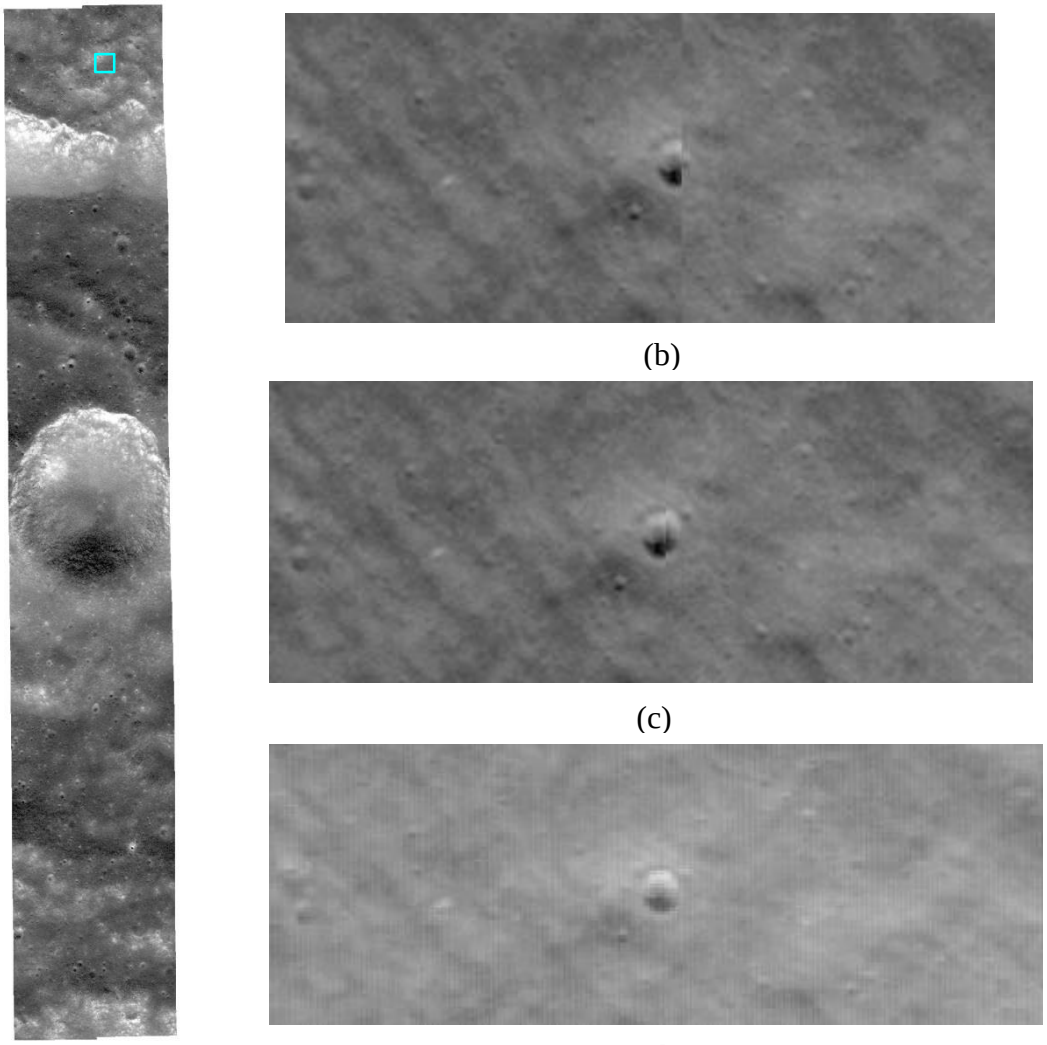

Figure 16. Comparison of orthorectified NACL and NACR image pair for image set 3. (a) Orthorectified image pair for the entire image (M170755060L/R), (b) a close-up view of the region marked with a cyan rectangle in (a) in the orthorectified image pair generated using the standard SPICE kernels, (c) using the temperature-dependent SPICE kernels, and (d) after calibration of boresight offsets.

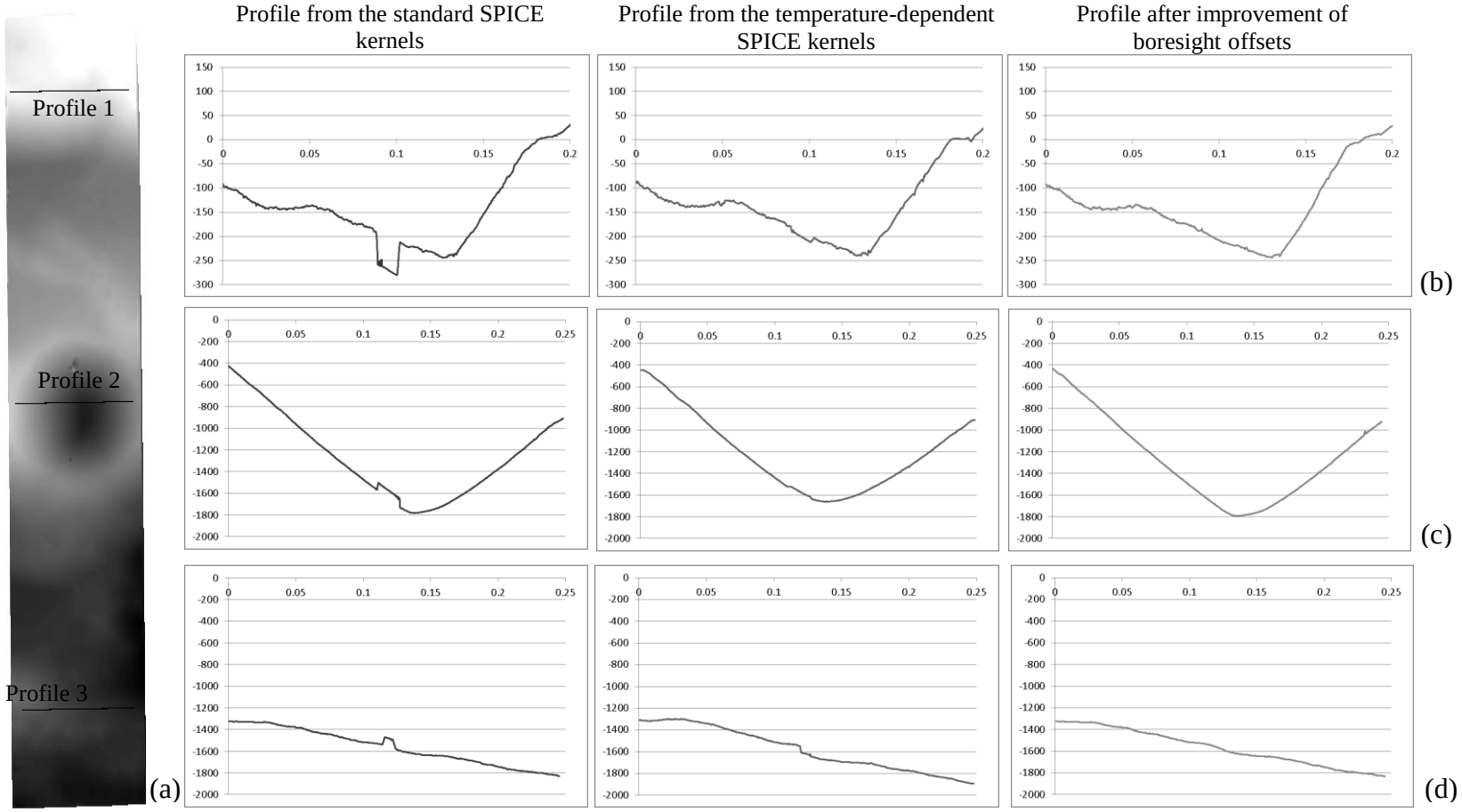

Figure 17. Profile comparison of the DEMs generated using different SPICE kernels for image set 3. (a) Three selected profiles marked on the planar view of the DEM, and comparisons for (b) profile 1, (c) profile 2, and (d) profile 3. (The units in the profile plots are meters of elevation for the vertical axis and degrees of longitude (with start point as 0°) for the horizontal axis)

Figure 17 shows the detailed profile comparison for this image set. It again clearly illustrates the performance of the proposed approach.

The improved angular boresight offsets from the proposed method for the three NAC stereo image sets used in the experiments are calculated. In average, the improved ω_b values are about 0.03° less than the preflight value of -2.765°, and the improved φ_b values are about 0.01° less than the preflight value of 0.106°. The improved κ_b values are in average 0.378° less than the preflight value of 180°, which is comparable to the 0.37° twist parameter found by Speyerer et al. (2014).

5. Conclusions and Discussion

This paper presents a method for calibration of boresight offsets of LROC NACs. The experimental results using typical NAC image sets and the analysis of the improved boresight offsets lead to the following conclusions:

1) Considerable changes in the relative boresight alignment between the two LROC NAC cameras do indeed exist during the operation of LRO orbiting the Moon in the extreme environments, which result in inconsistencies as great as 70 m in the generated DEMs when using the pre-flight derived SPICE kernels.
2) The temperature-dependent SPICE kernels recently released by the LROC team are useful to reduce the possible errors in the boresight parameters, and produce DEMs with better precision and internal consistency. However, internal inconsistencies of about 5 - 10 m still exist in the DEMs generated using the temperature-dependent SPICE kernels.
3) The proposed approach can effectively improve the boresight offsets between the NACL and NACR. With the proposed approach, large inconsistencies in object space in the generated DEMs can be significantly reduced to the meter level.

The results presented in this paper provide a useful check on the performance of the temperature-dependent SPICE kernels (Speyerer et al., 2014) of NAC imagery. It should be noted that this research focused only on the calibration of boresight offsets of LROC NACs for precision lunar topographic mapping. The proposed method can also be used in many other applications where stereo-photogrammetry is applied. For instance, when satellite images from multiple neighboring orbits are processed, similar approaches can be applied for accurate 3D mapping from them. And, nowadays there are more space-borne or airborne imaging systems with similar multiple camera systems for both high-resolution and large-coverage imaging capability. The proposed method can be extended and used in these applications.

Acknowledgments

This work was supported by a grant from the Research Grants Council of Hong Kong (Project No. PolyU 152086/15E), grants from the Hong Kong Polytechnic University (1-ZEA4, 4-BCBW, and G-YBA5), and grants from the National Natural Science Foundation of China (Project No. 41471345 and Project No. 41671426). The authors would like to thank the people who worked on the Planetary Data System archive for the LRO data sets to make the LROC NAC imagery publicly available.

References

Acton, C. H., 1996. Ancillary data services of NASA's navigation and ancillary information facility, Planetary and Space Science, vol. 44, pp. 65-70.

Bowman-Cisneros, E., 2010. LROC EDR/CDR Data Product Software Interface Specification, Arizona State University.

Burns, K. N., E. J. Speyerer, M. S. Robinson, T. Tran, M. R. Rosiek, B. A. Archinal, and E. Howington-Kraus, 2012. Digital Elevation Models and Derived Products from LROC NAC Stereo Observations, International Archives of the Photogrammetry, Remote Sensing and Spatial Information Sciences, vol. XXXIX-B4, pp. 483-488.

Di, K., Y. Liu, B. Liu, M. Peng, and W. Hu, 2014. A Self-calibration bundle adjustment method for photogrammetric processing of Chang'E-2 stereo lunar imagery, IEEE Transaction on Geoscience and Remote Sensing, vol. 52, no.9, pp. 5432-5442.

Li, R., W. Wang, S. He, L. Yan, X. Meng, J. Crawford, M.S. Robinson, T. Tran, and B.A. Archinal, 2011. Latest Results of 3D Topographic Mapping Using Lunar Reconnaissance Orbiter Narrow-Angle Camera Data, presented at the 42nd Lunar and Planetary Science Conference (LPSC), The Woodlands, TX, March 7-11.

Lin, L., 2012. Refined Geometric Processing of LROC NAC Stereo Imagery Based on the Rigorous Sensor Model, MSc Thesis, Ohio State University.

Mazarico, E., S. J. Goossens, F. G. Lemoine, G. A. Neumann, M. H. Torrence, D D. Rowlands, D. E. Smith, M. T. Zuber, 2013. Improved Orbit Determination of Lunar Orbiters with Lunar Gravity Fields Obtained by the GRAIL Mission, presented at the 44th Lunar and Planetary Science Conference, The Woodlands, TX, March 18-22.

Oberst, J., F. Scholten, K.-D. Matz, T. Roatsch, M. Wahlisch, I. Haase, P. Glaser, K. Gwinner, and M.S. Robinson, 2010. Apollo 17 Landing Site Topography from LROC NAC

Stereo Data – First Analysis and Results, presented at the 41st Lunar and Planetary Science Conference, The Woodlands, TX, March 7-11.

Robinson, M. S., S. M. Brylow, M. Tschimmel, D. Humm, S. J. Lawrence, P. C. Thomas, B. W. Denevi, E. Bowman-Cisneros, J. Zerr, M. A. Ravine, M A. Caplinger, F. T. Ghaemi, J. A. Schaffner, M. C. Malin, P. Mahanti, A. Bartels, J. Anderson, T. N. Tran, E. M. Eliason, A. S. McEwen, E. Turtle, B. L. Jolliff,·and H. Hiesinger, 2010. Lunar Reconnaissance Orbiter Camera (LROC) Instrument Overview, Space Science Reviews, vol. 150, no. 1-4, pp. 81-124.

Robinson, M. S., E. J. Speyerer, A. Boyd, D. Waller, R.V. Wagner, and K. N. Burns, 2012. Exploring the Moon with the Lunar Reconnaissance Orbiter Camera, International Archives of the Photogrammetry, Remote Sensing and Spatial Information Sciences, vol. XXXIX-B4, pp. 501-504.

Rosa, D., B. Bussey, J. T. Cahill, T. Lutz, I. A. Crawford, T. Hackwill, S. van Gasselt, G. Neukum, L. Witte, A. McGovern, P. M. Grindrod, and J. D. Carpenter, 2012. Characterisation of potential landing sites for the European Space Agency's Lunar Lander project, Planetary and Space Science, vol. 74, no.1, pp. 224-246.

Speyerer, E.J., R.V. Wagner, M.S. Robinson, A. Licht, P.C. Thomas, K. Becker, J. Anderson, S.M. Brylow, D.C. Humm, and M Tschimmel, 2014. Pre-flight and On-orbit Geometric Calibration of the Lunar Reconnaissance Orbiter Camera, Space Science Reviews, doi: 10.1007/s11214-014-0073-3.

Tran, T., M. Rosiek, R. Ross, A. Beyer, S. Mattson, E. Howington-Kraus, M. S. Robinson, B. A. Archinal, K. Edmundson, D. Harbour, and E. Anderson, 2010. Generating Digital Terrain Models Using LROC NAC Images, presented at the ASPRS/CaGIS 2010 Fall Specialty Conference, Orlando, FL, November 15-19.

Williams, J. G., D. H. Boggs, and W. M. Folkner, 2008. DE421 Lunar Orbit, Physical Librations, and Surface Coordinates, JPL Interoffice Memorandum 335-JW, DB.

Wu, B., J. Guo, Y. Zhang, B. King, Z. Li, and Y. Chen, 2011a. Integration of Chang'E-1 Imagery and Laser Altimeter Data for Precision Lunar Topographic Modeling, IEEE Transactions on Geoscience and Remote Sensing, vol. 49, no. 12, pp. 4889-4903.

Wu, B., Y. Zhang, and Q. Zhu, 2011b. A Triangulation-Based Hierarchical Image Matching Method for Wide-Baseline Images, Photogrammetric Engineering & Remote Sensing, vol. 77, no. 7, pp. 695-708.

Wu, B., Y. Zhang, and Q. Zhu, 2012. Integrated Point and Edge Matching on Poor Textural Images Constrained by Self-Adaptive Triangulations, ISPRS Journal of Photogrammetry and Remote Sensing, vol. 68, pp. 40-55.

Wu, B., J. Guo, H. Hu, Z. Li, and Y. Chen, 2013. Co-Registration of Lunar Topographic Models Derived from Chang'E-1, SELENE, and LRO Laser Altimeter Data Based on a Novel Surface Matching Method, Earth and Planetary Science Letters, vol. 364, pp. 68-84.

Wu, B., H. Hu, and J. Guo, 2014a. Integration of Chang'E-2 Imagery and LRO Laser Altimeter Data with a Combined Block Adjustment for Precision Lunar Topographic Modeling, Earth and Planetary Science Letters, vol. 391, pp. 1-15.

Wu, B., F. Li, L. Ye, S. Qiao, J. Huang, X. Wu, and H. Zhang, 2014b. Topographic Modeling and Analysis of the Landing Site of Chang'E-3 on the Moon, Earth and Planetary Science Letters, vol. 405, pp. 257-273.

Yoon, J.-S., and J. Shan, 2005. Combined Adjustment of MOC Stereo Imagery and MOLA Altimetry Data, Photogrammetric Engineering & Remote Sensing, vol. 71, no. 10, pp. 1179-1186.

Zhu, Q., B. Wu, and N. Wan, 2007. A Filtering Strategy for Interest Point Detecting to Improve Repeatability and Information Content, Photogrammetric Engineering & Remote Sensing, vol. 73, no. 5, pp. 547-553.

Zhu, Q., Y. Zhang, B. Wu, and Y. Zhang, 2010. Multiple Close-range Image Matching Based on a Self-adaptive Triangle Constraint, Photogrammetric Record, vol. 25, no. 132, pp. 437-453.